



HAL
open science

Mechanistic and Thermodynamic Insights into Anion Exchange by Green Rust

Myriam I Agnel, Sylvain Grangeon, François Fauth, Erik Elkaim, Francis Claret, Marjorie Roulet, Fabienne Warmont, Christophe Tournassat

► **To cite this version:**

Myriam I Agnel, Sylvain Grangeon, François Fauth, Erik Elkaim, Francis Claret, et al.. Mechanistic and Thermodynamic Insights into Anion Exchange by Green Rust. *Environmental Science and Technology*, 2020, 54 (2), pp.851-861. 10.1021/acs.est.9b05632 . hal-02488822

HAL Id: hal-02488822

<https://hal.science/hal-02488822v1>

Submitted on 2 Mar 2020

HAL is a multi-disciplinary open access archive for the deposit and dissemination of scientific research documents, whether they are published or not. The documents may come from teaching and research institutions in France or abroad, or from public or private research centers.

L'archive ouverte pluridisciplinaire **HAL**, est destinée au dépôt et à la diffusion de documents scientifiques de niveau recherche, publiés ou non, émanant des établissements d'enseignement et de recherche français ou étrangers, des laboratoires publics ou privés.

1 Mechanistic and thermodynamic insights into anion
2 exchange by green rust

3 *Myriam I. Agnel^{*,1}, Sylvain Grangeon^{1,2}, François Fauth³, Erik Elkaïm⁴, Francis Claret²,*
4 *Marjorie Roulet⁵, Fabienne Warmont⁵, Christophe Tournassat^{1,2,6}*

5 ¹ Univ. Orléans, CNRS, BRGM, ISTO, UMR 7327, F-45071, Orléans, France

6 ²BRGM, 3 Avenue Claude Guillemin, 45060 Orléans, France

7 ³CELLS – ALBA Synchrotron, Carrer de la Llum, 2-26, 08290 Cerdanyola del Vallès,
8 Barcelona, Spain

9 ⁴Synchrotron SOLEIL, L'Orme des Merisiers, 91190 Saint Aubin, France

10 ⁵ICMN, UMR 7374, CNRS/Université d'Orléans, 1 Rue de la Ferrollerie, 45071 Orléans, France

11 ⁶Energy Geoscience Division, Lawrence Berkeley National Laboratory, 1 Cyclotron Rd,
12 Berkeley, CA 94720, USA

13 KEYWORDS: Green rust, Anion exchange, Fougerite, Layered Double Hydroxide.

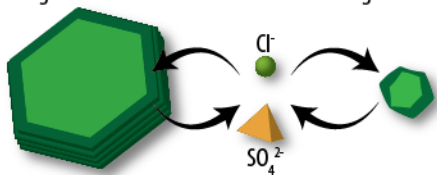
14

15 ABSTRACT

16 Fougérite is a naturally-occurring green rust, i.e. a layered double hydroxide (LDH) containing
17 iron (Fe). Fougérite was identified in natural settings such as hydromorphic soils. It is one of the
18 few inorganic materials with large anion adsorption capacity that stems from the presence of
19 isomorphic substitutions of Fe^{2+} by Fe^{3+} in its layers. The importance of anion adsorption in the
20 interlayer of LDH has often been highlighted, but we are still missing a mechanistic understanding
21 and a thermodynamic framework to predict anion uptake by green rust. We combined laboratory
22 and *in operando* synchrotron X-ray diffraction and scattering experiments with geochemical
23 modeling to contribute to filling this gap. We showed that the overall exchange process in green
24 rusts having nanometer and micrometer sizes can be seen as a simple anion exchange mechanism
25 without dissolution-recrystallization or interstratification processes. A thermodynamic model of
26 ion exchange, based on the Rothmund and Kornfeld convention, made it possible to predict the
27 interlayer composition in a large range of conditions. This multiscale characterization can serve as
28 a starting point for the building of robust and mechanistic geochemical models that will allow
29 predicting the role of green rust on the geochemical cycle of ions, including nutrients, in soils.

30 ABSTRACT ART

Micrometric & 3D-ordered
green rust Nanometric & turbostratic
green rust



Same layer structure
Same ion exchange mechanism
Different selectivity coefficient values

31
32

33 TEXT

34 INTRODUCTION

35 Green rust (GR) is a layered double hydroxide (LDH) that contains Fe^{2+} and Fe^{3+} , and which is
36 found both in engineered and natural environments.¹⁻³ Fougerite, the naturally-occurring form of
37 green rust, has been identified in several settings such as hydromorphic soils and river streams.^{1,4-}

38 ⁸ In the following “Fougerite” will be used to refer specifically to the mineral, while “green rust”
39 will be used both to refer to synthetic samples and to discuss properties that are common to
40 Fougerite and synthetic samples.

41 Where present, green rust exerts a strong influence on the mobility of nutrients, transition metals,
42 and actinides through adsorption, incorporation, and redox reactions.^{1,2,9-15} In addition, it is a
43 precursor of magnetite, which is another reactive mineral.^{1,12,16} As a consequence of its exceptional
44 reactivity, green rust is envisioned as a potential material for water treatment, either through
45 degradation or sorption of anionic contaminants.^{14,17} The sorption and redox properties of green
46 rust are due to its crystal structure. The ideal structural formula of green rust is $[\text{Fe}^{2+}_{(1-x)}\text{Fe}^{3+}_x(\text{OH})_2]^{+x} \cdot [x/n \text{ A}^{-n} \cdot m \text{ H}_2\text{O}]^{-x}$, where iron and hydroxyl groups form positively charged
47 layers, which are stacked and separated from each other by hydrated interlayer anions A^{-n} .^{1,3} n is
48 the charge of the anion, and m depends on factors such as relative humidity and nature of the
49 anion.^{15,18} Interlayer anions can undergo exchange reactions with the surrounding pore water, thus
50 explaining the anion sorption capability of these materials.^{2,14,15} Layers from natural and synthetic
51 samples also frequently contain isomorphic substitution of Fe^{2+} and Fe^{3+} by foreign cations such
52 as Al^{3+} , Mg^{2+} , Ni^{2+} , or Zn^{2+} .^{7,19,20} The sorption properties of green rust are thus apparently
53 analogous to the sorption properties of other layered minerals such as clay minerals (*e.g.* smectite)
54

55 or manganese oxides, but with an opposite permanent layer charge and sorption properties directed
56 towards anions instead of cations.^{21,22}

57 Inorganic materials with permanent anion adsorption capacity are scarce in nature, especially in
58 the pH range 7 to 9 that corresponds to the stability range of Fougerite.^{2,23} When present, this
59 mineral could have thus a major role in anions concentration buffering capacity in soils.¹⁵ While
60 it has been profusely demonstrated that clay minerals play a major part in the control of cation
61 retention and migration in soils, sediments and sedimentary rocks,²¹ the precise role of Fougerite
62 in the dynamics of anions in natural and engineered settings is less documented.²⁴ This can be
63 attributed, at least in part, to the scarcity or absence of quantitative data on anion exchange
64 reactions on green rust surfaces,^{2,3,25,26} which prevents a quantitative estimation using geochemical
65 modeling approaches. This paper intends to contribute filling this gap. Exchange processes on clay
66 minerals are usually quantified in the framework of the thermodynamic theory of ion exchange, in
67 which exchange selectivity coefficients are determined from batch adsorption/desorption
68 experiments.²¹ Literature studies carried out on a range of layered minerals and phases (e.g., clay
69 minerals, manganese oxides, or LDH phases present in cementitious materials) have shown
70 however that a sound understanding of the mechanisms of interactions between a layer and an
71 adsorbate of interest requires a molecular-scale description of the sorption process in order to
72 distinguish true reversible adsorption mechanisms from additional uptake mechanisms such as
73 structural incorporation or co-precipitation.^{2,27,28}

74 The objective of the present study was to develop a thermodynamic model for anion uptake in
75 green rust that is firmly grounded on molecular-scale foundations. Additionally, this development
76 included the quantification of the influence of particle crystallinity and size on sorption properties,
77 since previous studies proposed that these parameters may play a role.²⁹⁻³¹ In this view, we

78 synthesized two types of samples: a micrometric and defect-free green rust (micro-GR), and a
79 nanometric and turbostratic green rust (nano-GR), both having Cl^- as the interlayer anion. Then,
80 we characterized and quantified their sulfate (SO_4^{2-}) sorption mechanisms by combining laboratory
81 and synchrotron experiments. Cl^- and SO_4^{2-} were chosen because of their quantitative importance
82 in surficial waters, and because of their simple aqueous speciation.

83

84 **MATERIALS AND METHODS**

85 **Anoxic conditions.** All synthesis steps and laboratory experiments were conducted in a glove
86 box (MBraun UNIlab Pro) filled with a N_2 atmosphere in order to prevent the oxidation of green
87 rust by atmospheric O_2 . All solutions were prepared with O_2 -free ultrapure water (resistivity of
88 $18.2 \text{ M}\Omega\cdot\text{cm}$) and analytical grade salts. The glove box O_2 volumetric concentration was regularly
89 monitored and did not exceed 0.1 Pa . Samples used for synchrotron experiments were sealed in
90 airtight containers in the glove box. They were stored in another N_2 atmosphere glove boxes at the
91 synchrotron facilities until being used for the experiments.

92

93 **Green rust samples.** The samples were synthesized using a previously published method.³²
94 Briefly, a FeCl_2 solution ($50 \text{ g}\cdot\text{L}^{-1}$) was mixed with another one of hexamminecobalt(III) chloride
95 (CoHex , $10 \text{ g}\cdot\text{L}^{-1}$). Two samples were synthesized by varying the ratio of FeCl_2 to CoHex so as
96 to produce a turbostratic and nanometric green rust, hereafter named nano-GR(Cl), and a defect-
97 free and micrometric green rust, hereafter named micro-GR(Cl). Turbostratism is defined by the
98 systematic occurrence of random translations parallel to the layers and/or rotations about the
99 normal direction to the layers between successive layers. The solid aged for three days before
100 filtration ($0.22 \mu\text{m}$) of the dispersion. This synthesis method did not require external control on

101 the pH, which reached green rust equilibrium pH as soon as the solid precipitated (pH range during
102 synthesis for nano-GR(Cl)=8.3-8.6, and micro-GR(Cl)=8-8.2).³² No additional washing was done
103 before the solid samples were dried for one day in order to minimize side reactions, including
104 dissolution, that could have been induced by the sharp changes in chemical conditions, which
105 always occur during washing procedures.

106 The present synthesis method was chosen because it allowed for a fine-tuning of the size and
107 amount of stacking defects. The drawback of the method was the partial substitution of Fe²⁺ by
108 Co²⁺ in the layer.³² However, this was not considered to be a problem because (i) the
109 crystallographic structure of the synthesized solids was almost identical to that of Fougerite (Fig.
110 S5), (ii) the layer charge was not influenced by the Fe²⁺ versus Co²⁺ substitution, and (iii) Fougerite
111 has never been observed as a pure Fe²⁺/Fe³⁺ phase in natural environments, because of isomorphic
112 substitutions of Fe by foreign cations such as Mg, Ni, or Zn.^{7,13,33}

113
114 **Determination of layer structural formula and interlayer anion content.** The
115 structural formula of the studied samples was $[\text{Fe}^{2+}_{1-x-y}\text{Fe}^{3+}_x\text{Co}^{2+}_y (\text{OH})_2]^{+x} \cdot [x/n \text{A}^{-n} \cdot m\text{H}_2\text{O}]^{-x}$,
116 where A⁻ⁿ=Cl⁻ or SO₄²⁻.³² The values of x and y , which can vary between 0 and 1, were calculated
117 from electron probe micro-analyzes (EPMA; Cameca SX Five electron microprobe). Analyses
118 were carried out on freeze-dried samples embedded in epoxy mounts. After polishing the epoxy
119 mount, a 10-20 nm thick carbon layer was sputter-coated on the samples. Acceleration voltage was
120 15 kV, beam current was 10 nA and beam width was 1-2 μm. Fe Kα and Co Kα were analyzed
121 using a LiF (Lithium Fluoride) crystal, while Cl Kα and SO₄ Kα were analyzed with a LPET (Large
122 Pentaerythritol) and a PET (Pentaerythritol) crystal respectively. Pyrite, metallic Co, Vanadinite
123 and Celestite were used as standards for Fe, Co, Cl and SO₄ respectively. Counting times was set

124 to 30 s for all elements. Depending on the sample, the number of independent measurements
125 ranged 35-61. In order to provide additional constraints on the chemical formula, the total Fe
126 content was also quantified with a modified 1,10-phenanthroline method.³²

127
128 **Determination of the water content.** The water content (m) was determined with
129 thermogravimetric analyses (TGA) and differential thermal analysis (DTA). Samples were dried
130 for one day in the glove box, before measurement on a Setaram TGA 92-16.18 under an Argon
131 flux. Approximately 50 mg of powder were heated from 20 °C to 500 °C at 1 °C min⁻¹. Then, the
132 temperature was maintained at 500 °C for 1 h before cooling. The mass loss attributed to water
133 vaporization during the TGA measurement (ΔTG) was linked to the value of m according to:

$$m = \frac{M_{GR}}{M_w} \times \frac{\Delta TG}{m_{GR}} \quad (1)$$

134 where M_{GR} is the molar mass of the anhydrous GR (*i.e.* considering $m=0$), m_{GR} is the mass of the
135 anhydrous sample, and M_w is the molar mass of water. Care was taken to avoid any contact with
136 atmospheric CO₂ during sample transportation and analysis.

137
138 **Transmission Electron Microscopy (TEM).** TEM samples were prepared according to
139 two different methods. In the first method, solid powders were dispersed into ultrapure water using
140 an ultrasonic bath, and then deposited on lacey carbon films loaded on copper grids. In order to
141 avoid as much as possible oxidation, samples were preserved in a glovebox until a quick
142 preparation (< 5 min) under open air. Samples were then directly inserted in the TEM. In the
143 second method, samples were embedded in Agar 100 resin and left for polymerization for 2 days
144 in the dark. Then, 80 nm thick slices were prepared with an ultramicrotome (Reichert-Jung Ultra-

145 cut E) equipped with a diamond knife. The slices were deposited on lacey carbon films loaded on
146 copper grids. TEM data were acquired using a Philips CM20 operated at 200 kV.

147

148 **Diffraction characterization of the solid phase.** Two types of synchrotron
149 experiments were conducted. In the first type, X-ray diffraction data (XRD) were recorded during
150 in situ and time-resolved sorption experiments conducted on beamline MSPD (ALBA
151 Synchrotron, Barcelona, Spain).^{34,35} The X-ray wavelength (λ) was 0.8258 Å (15 keV). Data were
152 collected with a Mythen detector. Green rust was loaded in polyimide capillaries sealed on both
153 extremities using a frit-in-a-ferrule system (IDEX Health & Science).³⁶ At the beginning of each
154 experiment, a capillary was connected on one-side to a peristaltic pump and to the other side to a
155 sampling pot, using silicon tubing. The flow rate of the pump was 1-2 mL·h⁻¹. In a first step
156 (equilibrium step), the sample was hydrated by flowing a solution of 50 mmol·L⁻¹ NaCl at pH 8.
157 In a second step (exchange step), a solution of 5 mmol·L⁻¹ Na₂SO₄ and 40 mmol·L⁻¹ NaCl at pH 8
158 was flowed through the capillary. A diffraction pattern was acquired every 15 s during both steps.
159 The crystallite size was calculated using Scherrer's law (see Supplementary Data).³⁷ Rietveld
160 refinements were carried out on micro-GR(Cl) with the Fullprof software,³⁸ using the structure
161 models from Fougerite and magnetite.^{7,39} The quality of the data modelling was quantified using
162 the R_{exp} , R_p , R_{wp} , and goodness-of-fit (GoF) parameters, where R_p is the unweighted residual error,
163 R_{wp} is the weighted residual error, R_{exp} is the lowest R_{wp} that can be achieved as a result of
164 statistical noise on the data, and GoF is the squared R_{wp} to R_{exp} ratio.⁴⁰

165 The second type of synchrotron experiments involved processing the high-energy X-ray
166 scattering data of dried samples collected, at beamline CRISTAL from the SOLEIL synchrotron
167 (Paris, France) and using previously developed methods.^{36,41} The energy was 28 keV ($\lambda = 0.4367$

168 Å). An XPad hybrid pixel detector collected data between 1.2-124.5° 2 θ angular range with a total
169 collection time of 30 min. Then, data were processed with the software FUSION⁴² and Fourier
170 transformed to X-ray Pair Distribution Function (PDF) data with *PDFgetX3*.⁴³ Systematic random
171 stacking disorder (turbostratism disorder) affects the PDF by cancelling out the contribution from
172 atomic pairs formed from atoms located on distinct layers. To assess quantitatively this effect, two
173 PDF were calculated. The first one, which served as a model PDF for an ordered and micrometric
174 green rust, was calculated using the Fougerite structure model,⁷ in which the number of water
175 molecules and *a* and *b* lattice parameters were adjusted to match data acquired with independent
176 methods, and in which the occupancy of layer O was set to 1. The second calculated PDF aimed
177 at mimicking the PDF of a turbostratic and nanosized green rust. For this purpose, a structure
178 model was created, in which a single Fougerite sheet was isolated in a lattice cell with *a* and *b*
179 dimensions identical to that of the ordered Fougerite but with *c* dimension expended to 30 Å to
180 cancel any correlations related to atoms located on distinct layers in the calculated PDF (up to 30
181 Å). Note that the relative atomic coordinates of all atoms were corrected correspondingly, so that
182 the layer structure remained unaffected by this operation. The drawback of using such a
183 “supercell” approach was the significant lowering of the electronic density in the cell, ρ , compared
184 to that of an actual turbostratic sample. This effect manifested itself in the calculated PDF with an
185 underestimation of the slope at low *r* values, which is a function of ρ .⁴⁰ However, this did not affect
186 the position nor the intensity of correlations, which could be compared safely to other calculated
187 or experimental data. The size of the crystallites was set to 50 Å using the “spdiameter” from
188 PDFgui. For both structures, the u_{11} , u_{22} and u_{33} anisotropic displacement parameters of Fe were
189 0.01 Å and those of interlayer species were 0.1 Å. u_{11} and u_{22} of layer O were also 0.01, but u_{33}

190 was set to 0.03 Å to match experimental data. Such increase in u_{33} of layer O was also observed
191 for several other layered phases,^{28,36,41,44,45} and is possibly related to layer corrugation.

192

193 **Cl⁻ – SO₄²⁻ exchange experiments.** NaCl and NaSO₄ stock solutions as well as mixes of
194 these solutions were prepared so as to reach a constant Na concentration of 50 mmol·L⁻¹, and a pH
195 value between 7 and 8. Green rust samples were dried again for one day prior to experiments.
196 During the pre-conditioning step, about 0.2 g of nano-GR(Cl) or 0.5 g of micro-GR(Cl) were
197 equilibrated with 200 mL of a 50 mmol·L⁻¹ NaCl solution for 30 min. Then, the solution and the
198 solid were separated by filtration (cut-off diameter of 0.22 μm). The solid was rinsed with 30-40
199 mL of O₂- and CO₂-free ultrapure water, and then filtrated.

200 During each of following steps, except rinsing, the green rust was dispersed in the solutions
201 during 30 min, which was sufficient to attain steady state conditions for Cl⁻ and SO₄²⁻
202 concentrations based on in-situ XRD measurements of Cl⁻-SO₄²⁻ exchange experiments. In a first
203 series of experiment, the green rust samples were re-dispersed with a 25 mmol·L⁻¹ Na₂SO₄ solution
204 and then filtrated. Three dispersion-filtration steps were carried out. The objective of this series of
205 experiments was the characterization of the Cl⁻– SO₄²⁻ reaction stoichiometry, with the comparison
206 of SO₄²⁻ uptake and Cl⁻ release in a single step, as well as of the anion exchange capacity (AEC),
207 with the measurement of the total amount of Cl⁻ released by the sample. In a second series of
208 experiments, the solid was re-dispersed with solutions containing Cl⁻ and SO₄²⁻ with a total Na⁺
209 concentration of 50 mmol·L⁻¹ and then filtrated. Again, five to six dispersion-filtration steps were
210 carried out. After those 5 to 6 steps, the solid was rinsed with a known volume of ultrapure water,
211 and dispersed again with a 25 mmol·L⁻¹ Na₂SO₄ solution and filtrated (one to two dispersion-
212 filtration steps). The objectives of this second set of experiments were to calculate equivalent

213 fractions and to determine the ion exchange thermodynamic convention and, accordingly, to
 214 calculate selectivity coefficients. All details about solution concentrations and volumes are
 215 available in the electronic annex (Table S1 to S3). The mass of the filtrated solutions and their Cl⁻
 216 and SO₄²⁻ concentrations were quantified by High-Performance Liquid Chromatography (HPLC;
 217 Thermo Scientific Dionex ICS-3000) at each step in order to determine the concentration of Cl⁻
 218 and SO₄²⁻ in the solution, as well as in the solid by cumulative difference with the initial solid
 219 concentration.

220

221 **Geochemical modeling.** Experimental results were modelled with PHREEQC⁴⁶ in order to
 222 determine the selectivity coefficient (K_{ex}) of the exchange reactions. At each step, the solution was
 223 assumed to be at equilibrium with the anion exchanger composition, according to the reaction:



224 where A⁺ represents the anion exchanger. The ion exchange thermodynamic convention of
 225 Rothmund and Kornfeld was used to compute the exchanger composition as a function of the
 226 solution composition:^{21,47}

$$K_{ex,RK} = \frac{(\text{Cl}^-)^2}{(\text{SO}_4^{2-})} \left(\frac{E_{\text{SO}_4}}{E_{\text{Cl}}^2} \right)^{1/\beta} \quad (3)$$

227 where values in round brackets represent activities in solution, β is an empirical parameter, and E_i
 228 is the equivalent fraction of ion i on the exchanger:

$$E_{\text{SO}_4} = \frac{2[\text{A}_2\text{SO}_4]}{2[\text{A}_2\text{SO}_4] + [\text{ACl}]} \quad (4)$$

$$E_{\text{Cl}} = \frac{[\text{ACl}]}{2[\text{A}_2\text{SO}_4] + [\text{ACl}]} = 1 - E_{\text{SO}_4} \quad (5)$$

229 The value of the Gaines and Thomas selectivity coefficient ($K_{ex,GT}$) is related to the Rothmund
230 and Kornfeld selectivity coefficient with:

$$K_{ex,GT} = K_{ex,RK} \left(\frac{(1 - E_{SO_4})^2}{E_{SO_4}} \right)^{\frac{1}{\beta} - 1} \quad (6)$$

231 The Rothmund and Kornfeld model is equivalent to the Gaines and Thomas thermodynamic
232 convention in the case of $\beta=1$.^{21,47}

233

234

235 RESULTS AND DISCUSSION

236 Structural formula and anion exchange capacity of micro- and nano-GR

237 **samples.** According to EPMA (Table S4 in supplementary data), the structural formula of micro-

238 GR(Cl) was $[\text{Fe}^{2+}_{0.42(8)}\text{Fe}^{3+}_{0.25(4)}\text{Co}^{2+}_{0.33(4)}(\text{OH})_2] \cdot \text{Cl}^{-}_{0.25(4)} \cdot m\text{H}_2\text{O}$, and that of nano-GR(Cl) was

239 $[\text{Fe}^{2+}_{0.29(6)}\text{Fe}^{3+}_{0.20(3)}\text{Co}^{2+}_{0.51(5)}(\text{OH})_2] \cdot \text{Cl}^{-}_{0.20(3)} \cdot m\text{H}_2\text{O}$ with m the stoichiometry for water molecules.

240 The amounts of Fe deduced from these formulas, *i.e.* 7.97 mmol·g⁻¹ for micro-GR(Cl) and 4.63

241 mmol·g⁻¹ for nano-GR(Cl), compared well with those obtained with the 1,10-phenanthroline

242 method (7.34 mmol·g⁻¹ and 4.69 mmol·g⁻¹ respectively). After exchange with SO_4^{2-} , structural

243 formulas became $[\text{Fe}^{2+}_{0.44(4)}\text{Fe}^{3+}_{0.22(2)}\text{Co}^{2+}_{0.34(2)}(\text{OH})_2] \cdot \text{SO}_4^{2-}_{0.11(1)} \cdot m\text{H}_2\text{O}$ and

244 $[\text{Fe}^{2+}_{0.37(5)}\text{Fe}^{3+}_{0.16(2)}\text{Co}^{2+}_{0.48(3)}(\text{OH})_2] \cdot \text{SO}_4^{2-}_{0.08(1)} \cdot m\text{H}_2\text{O}$ for micro-GR(SO_4) and nano-GR(SO_4)

245 respectively. The transformation of nano-GR(Cl) and micro-GR(Cl) samples into their sulfate

246 forms, nano-GR(SO_4) and micro-GR(SO_4) respectively, did not change significantly their layer

247 composition, and involved a replacement of two Cl^- ions by one SO_4^{2-} ion.

248 TGA measurements gave similar results for the nano-GR(Cl) and the micro-GR(Cl) samples

249 (Fig. 1 and S1 to S3 in supplementary data). From room temperature to 140-150 °C, a mass loss of

250 ~15 % was attributed to interparticle (capillary) pore water.⁴⁸ The additional ~5 % mass loss from
 251 150 °C to 250 °C was attributed to interlayer water.^{9,48-50} Mass losses were endothermic, thus
 252 supporting a water vaporization mechanism. The TGA results for nano-GR(SO₄) were similar as
 253 for nano-GR(Cl) (Fig S2). Interparticle water was evaporated between 20 and 180 °C with a mass
 254 loss of ~15 % and interlayer water from 180 to 230 °C with a mass loss of ~5 %. For micro-
 255 GR(SO₄), the first mass loss was ~10 % from 20 to 140 °C (Fig S3). The second mass loss was
 256 also 10 % from 140 °C to 310 °C. The latter temperature was much higher than the upper
 257 temperature obtained for the second mass loss of micro-GR(Cl) (240 °C). In addition, the process
 258 began to be exothermic at 140 °C, which questioned the interpretation of vaporization of interlayer
 259 water. In the following, we attributed, nonetheless, the mass loss entirely to interlayer water.

260 The following structural formulas were obtained with *m* calculated from Eq. (1):

261 $\text{Fe}^{2+}_{0.42(8)}\text{Fe}^{3+}_{0.25(4)}\text{Co}^{2+}_{0.33(4)}(\text{OH})_2] \cdot \text{Cl}^{-}_{0.25(4)} \cdot (\text{H}_2\text{O})_{0.43}$ for micro-GR(Cl),

262 $[\text{Fe}^{2+}_{0.29(6)}\text{Fe}^{3+}_{0.20(3)}\text{Co}^{2+}_{0.51(5)}(\text{OH})_2] \cdot \text{Cl}^{-}_{0.20(3)} \cdot (\text{H}_2\text{O})_{0.40}$ for nano-GR(Cl),

263 $[\text{Fe}^{2+}_{0.44(4)}\text{Fe}^{3+}_{0.22(2)}\text{Co}^{2+}_{0.34(2)}(\text{OH})_2] \cdot \text{SO}_4^{2-}_{0.11(1)} \cdot (\text{H}_2\text{O})_{0.6}$ for micro-GR(SO₄) and

264 $[\text{Fe}^{2+}_{0.37(5)}\text{Fe}^{3+}_{0.16(2)}\text{Co}^{2+}_{0.48(3)}(\text{OH})_2] \cdot \text{SO}_4^{2-}_{0.08(1)} \cdot (\text{H}_2\text{O})_{0.23}$ for nano-GR(SO₄). Numbers within

265 brackets are the uncertainty on the last digit, calculated as the standard deviation of the mean value.

266 One of the key parameters for the quantitative understanding of LDH reactivity is the

267 determination of the anion exchange capacity that is representative of the quantity of anion that

268 can be adsorbed by a given mass of LDH. It was first calculated from the structural formula of the

269 fresh samples (assuming that all Cl⁻ was exchangeable) and that of the reacted samples (assuming

270 that all SO₄²⁻ was exchangeable). Because of the importance of this parameter, the AEC was also

271 calculated from the quantity of Cl⁻ leached by a weighted amount of green rust during the exchange

272 with a 25 mmol·L⁻¹ Na₂SO₄ solution. Although some variability was observed, all results

273 coherently pointed out to an AEC of two moles of electric charge per kilogram of anhydrous green
274 rust ($\text{mol}_c \cdot \text{kg}_{\text{anhydrous GR}}$, Table 1).

275

276 **Structure of micro- and nano-GR samples.** The micro-GR(Cl) XRD pattern had
277 numerous sharp and symmetrical peaks, which were modeled successfully with the Fougerite
278 structure and a minor amount of magnetite (14 % - $R_{\text{wp}} = 33\%$, $R_{\text{exp}} = 8\%$, $\text{GoF} = 17$ – Fig. S4). The
279 sole significant difference with the Fougerite model of Trolard et al.⁷ was a 4-fold increase in the
280 quantity of interlayer water, which was explained by the different hydration state of our samples
281 during measurement. Layer symmetry was hexagonal, and could be described with a system were
282 $a = b = 3.1640 \text{ \AA}$ and $\gamma = 120^\circ$. The sole symmetrical reflection found in the nano-GR(Cl) XRD
283 pattern were at $q=0.80$ and 1.59 \AA and match Fougerite $00l$ reflections (Fig. S5). All other
284 reflections were broad, most of them were asymmetrical, and their intensity was low as compared
285 to peaks observed in micro-GR(Cl). Broadening was attributed to nanocrystallinity. However, the
286 XRD pattern of nano-GR(Cl) was incompatible with a nanometric and 3D-ordered green rust, for
287 which Bragg peaks would be extremely broad yet still present (Fig. S6). The asymmetrical peaks
288 of low intensity were diagnostic for turbostratic disorder.^{51,52} Indeed, the XRD pattern of
289 turbostratic structure only contain $00l$ reflections and unsolved hk bands.⁵² In turbostratic layered
290 Mn oxides, which have a layer structure very close to green rust and an XRD pattern that is very
291 similar to that observed here for nano-GR(Cl), two layer symmetries have been described. The
292 first one is the hexagonal symmetry that can be described equally with $a = b$ and $\gamma = 120^\circ$ or with
293 the equivalent $a = \sqrt{3} \times b$, $\gamma = 90^\circ$ system (Fig S7), and the second one is the orthogonal layer
294 symmetry ($a > \sqrt{3} \times b$ and $\gamma = 90^\circ$).⁵³ Hexagonal and orthogonal layer symmetries can be
295 distinguished from the ratio of the d -spacing of the 11,20 and 31,02 bands (using an indexing with

296 $\gamma = 90^\circ$) and the shape of the 31,02 band: in the hexagonal layer symmetry, it is equal to $\sqrt{3}$, and
297 the 31,02 band is almost symmetrical. In this study, the ratio of the d -spacing of the two bands at
298 $q = 2.34 \text{ \AA}^{-1}$ and $\sim 4.03 \text{ \AA}^{-1}$, assigned to be the 11,20 and 31,02 bands, respectively, was 1.72, close
299 to $\sqrt{3}$. Consequently, nano-GR had, like micro-GR, hexagonal layer symmetry.^{36,53,54} This
300 observation reinforced the hypothesis of nano-GR(Cl) being a nanometric and turbostratic
301 variation of micro-GR(Cl).

302 Despite the distinctive shapes of micro-GR(Cl) and nano-GR(Cl) XRD patterns, the PDF of both
303 samples were overlaid for r values lower than 5.95 \AA , which corresponds to the layer-to-layer
304 distance of a green rust containing interlayer Cl^- (7.95 \AA) minus the layer thickness (2 \AA , Fig. 2A).
305 Because the area of a PDF correlation is directly proportional to the number of atoms involved in
306 the correlation and to their nature,⁴⁰ this overlay at low r values indicated that nano- and micro-
307 GR(Cl) had the same layer structure, and further supported the hypothesis of nano-GR(Cl) being
308 a disordered (turbostratic) variation of micro-GR(Cl). At r values higher than 5.95 \AA , several
309 correlations that were present in the PDF of the micro-GR(Cl) sample were absent in the PDF of
310 the nano-GR(Cl) sample. The same correlations were present in the calculated Fougerite PDF,
311 whereas they were absent in the calculated PDF of a single Fougerite sheet (Fig. 2B). Calculation
312 of a partial PDF showed that these missing correlations were attributable to Me-Me atomic pairs
313 (Fig. 2A, Me = $\text{Fe}^{2+,3+}$, Co^{2+}) with the two atoms being located in distinct layers, because they
314 were absent in the calculated PDF of a single Fougerite layer (Fig. 2C). In contrast, the Me-Me
315 pairs that were observed in the two calculated PDF (e.g., at 8.02, 12.25, 12.1-12.3, and 15 \AA – Fig.
316 2A), and that could thus be attributed to Me-Me atomic pairs within a given layer, were also
317 observed in the experimental PDF of both nano-GR(Cl) and micro-GR(Cl). Finally, the Me-Me
318 correlations gradually shifted towards low r values with increasing r in the PDF of nano-GR(Cl)

319 relative to those of micro-GR(Cl). Consequently, the in-plane lattice parameters of nano-GR(Cl)
320 were slightly smaller than those of micro-GR(Cl). Nano-GR(Cl) layers had a higher $\text{Co}^{2+}/\text{Fe}^{2+}$
321 ratio than micro-GR(Cl), and the ionic radius of Co^{2+} is $\sim 5\%$ smaller than that of Fe^{2+} in octahedral
322 coordination.⁵⁵ Thus, the smaller values of in-plane lattice parameters for nano-GR(Cl) compared
323 to micro-GR(Cl) were consistent with this difference in layer composition. The PDF of nano-
324 GR(Cl) canceled at $r \sim 50 \text{ \AA}$, whereas several intense correlations were present at higher r values
325 in the PDF of micro-GR(Cl), consistent with nano-GR(Cl) being nanocrystalline, and micro-
326 GR(Cl) being microcrystalline. Such hypothesis was confirmed by a Fourier transform of the $r >$
327 50 \AA part of the PDF, where no signal attributable to the sample could be detected for nano-GR(Cl)
328 (data not shown). PDF results were thus in agreement with our interpretation of XRD data.

329 TEM images evidenced two distinct morphologies for nano-GR(Cl) and micro-GR(Cl)
330 (Fig. Figure 3). Nano-GR(Cl) crystals were systematically aggregated and xenomorphic. Micro-
331 GR(Cl) crystals were automorphic and their size in the **a-b** plane varied between 0.1 and 1 μm
332 with a maximum thickness along \mathbf{c}^* of 40 nm. Thus, only the morphology of micro-GR(Cl) could
333 be determined with confidence. Layer-to-layer distances, deduced from a Fast Fourier transform
334 () analysis of the images, were: 7.1 \AA for nano-GR(Cl) and 7.4 \AA for micro-GR(Cl). Those values
335 were lower than the layer-to-layer distances deduced from XRD analysis due to TEM conditions.

336

337 **Mechanism of transformation from GR(Cl) to GR(SO₄).** Na_2SO_4 and NaCl solution
338 was flowed through nano- and micro-GR(Cl), thus transforming them to GR(SO₄). During this
339 exchange, the intensity of the X-ray reflection at $q = 0.78 \text{ \AA}^{-1}$ (equivalent to a d -spacing of 7.95
340 \AA) steadily decreased with time, while a reflection appeared and increased in intensity at 0.57 \AA^{-1}
341 ($d = 11.02 \text{ \AA}$; Fig. 4). Concomitantly, almost all peaks present at higher q values in the XRD

342 pattern of micro-GR also shifted, with the noticeable exception of those having $hk0$ indices (e.g.,
343 the 110 reflection at $q = 3.89 \text{ \AA}^{-1}$). This was most straightforwardly explained by an increase in c
344 during the experiment, while a and b remained unaffected. For nano-GR, only $00l$ reflections were
345 shifting. At higher q values, the position of all hk bands remained unchanged, consistent with c
346 increasing and a and b remaining constant. However, the shape of the high- q side of the 11,20
347 band at 2.34 \AA^{-1} evolved. This was due to a change in the nature, location and (or) density of the
348 atoms in the lattice,⁵² consistent with an anion exchange.

349 The increase in c in both samples was consistent with the replacement of Cl^- by SO_4^{2-} in the
350 interlayer. The $00l$ reflections of nano- and micro-GR(Cl) and of nano- and micro-GR(SO_4)
351 remained symmetrical and did not exhibit significant width changes during the experiment. In
352 addition, every reflection of hkl indices with $l \neq 0$ changed from the position corresponding to the
353 Cl^- variation to the position corresponding to the SO_4^{2-} variation without a gradual shift and without
354 the appearance of a peak at an intermediate position. Finally, the average crystallite size remained
355 constant throughout the experiments (Figs. 4D). Collectively, these observations showed that a
356 simple anion exchange mechanism occurred without dissolution-recrystallization processes, and
357 that an interstratification phenomenon (*i.e.* ordered or disordered alternations of Cl^- and SO_4^{2-}
358 interlayers within a given crystal) was also unlikely.⁵¹

359

360 **Cation exchange selectivity coefficient.** $\text{Cl}^- - \text{SO}_4^{2-}$ exchange data could not be modeled
361 with an ion exchange model using a constant selectivity coefficient and using the usual exchange
362 conventions of Vanselow, Gaines and Thomas, or Gapon.^{21,56} With these ion exchange
363 conventions, it was necessary to increase the value of the selectivity coefficient with an increase
364 of SO_4^{2-} occupancy in the exchanger. Such changes of selectivity coefficient values as a function

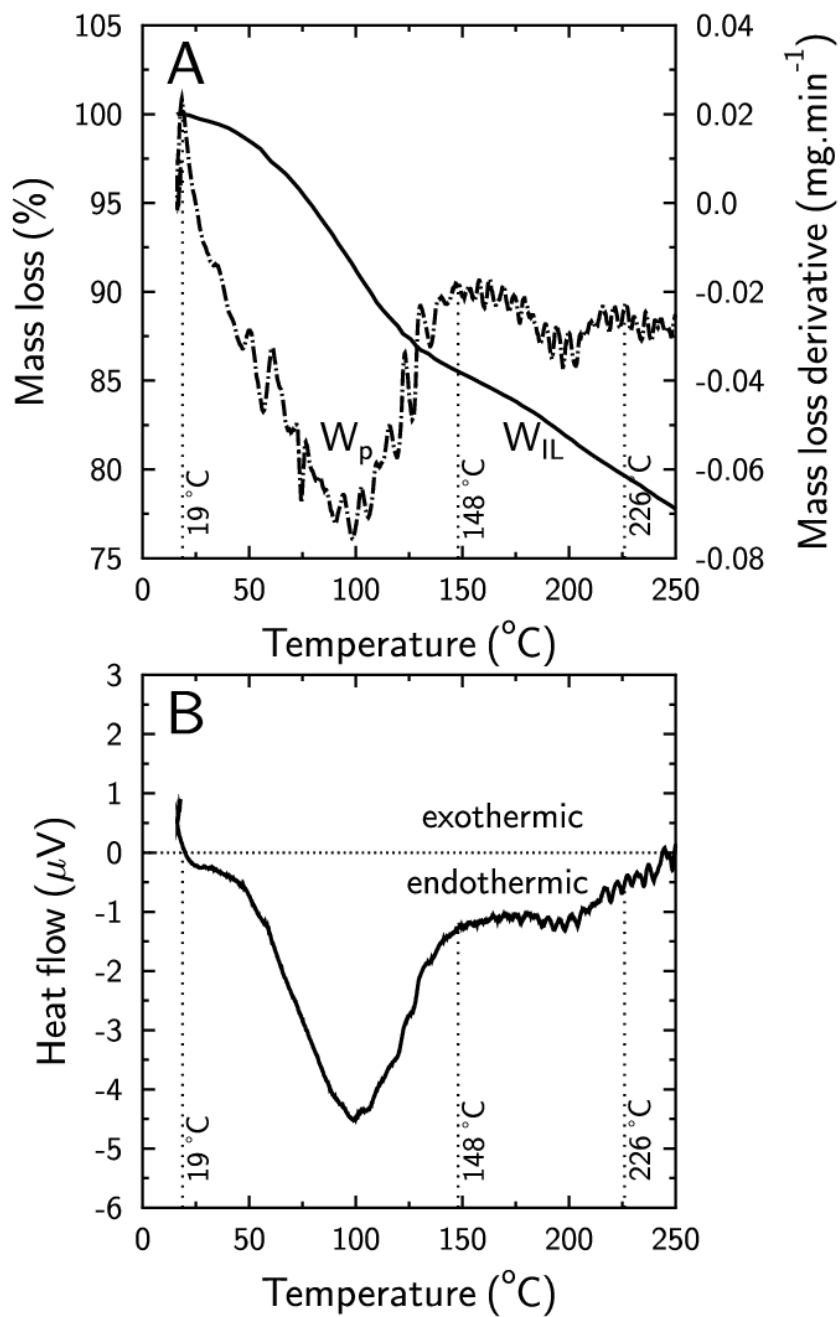
365 of chemical conditions are usually well captured with a Rothmund and Kornfeld model (Eq.
366 (3)).^{21,47} Indeed, an acceptable fit of the data was obtained with a $\log_{10} K_{ex,RK}$ value of 0.3 and a β
367 value of 2.4 for the micro-GR sample (Fig. 5), and with a $\log_{10} K_{ex,RK}$ value of 0.2 and a β value of
368 5 for the nano-GR sample (Fig. 6). The model predicted that 86 % and 95 % of the exchange sites
369 were occupied by SO_4^{2-} in the micro-GR and nano-GR samples respectively, at equilibrium with
370 an aqueous solution containing 40 $\text{mmol}\cdot\text{L}^{-1}$ Cl^- and 5 $\text{mmol}\cdot\text{L}^{-1}$ SO_4^{2-} . These results were in
371 agreement with XRD data that showed that Cl^- interlayers were only a minor component after
372 equilibration of the sample with this aqueous solution (Fig. 4).

373 The values of β were larger than one, meaning that the Gaines and Thomas selectivity coefficient
374 $K_{ex,GT}$ of the $\text{Cl}^- \rightarrow \text{SO}_4^{2-}$ exchange reaction increased with the SO_4^{2-} occupancy on the exchanger.
375 A large increase of the A \rightarrow B selectivity coefficient with an increase of the exchanger occupancy
376 by species B is at variance with observations made on cationic clays for which the reverse tendency
377 has been observed frequently. The decrease of the selectivity in clays is usually linked to the
378 presence of several types of adsorption sites with decreasing affinities for the species B compared
379 to species A.⁵⁷⁻⁶¹ Consequently, the mechanism of anion exchange in green rust interlayers may
380 be different from ion exchange in cationic clay minerals interlayers. Miyata observed also a
381 monotonous increase of the $\text{NO}_3^- \rightarrow \text{Br}^-$ selectivity coefficient with the Br^- exchanger occupancy on
382 Mg-Al hydrotalcite-like compounds (Mg-Al LDH).⁶² Because of the similarities of structure
383 between Mg-Al LDH and green rust, we speculate that the peculiar anion exchange properties of
384 green rust could be related to the structuration of anions in the interlayer, which is influenced by
385 the geometry of the anion (spherical and point charge for Cl^- , tetrahedral oxyanion for sulfate), the
386 high charge density (0.18 $\text{C}\cdot\text{m}^{-2}$ for micro-GR compared to -0.11 $\text{C}\cdot\text{m}^{-2}$ for Wyoming
387 montmorillonite) and the high surface occupation.^{20,63}

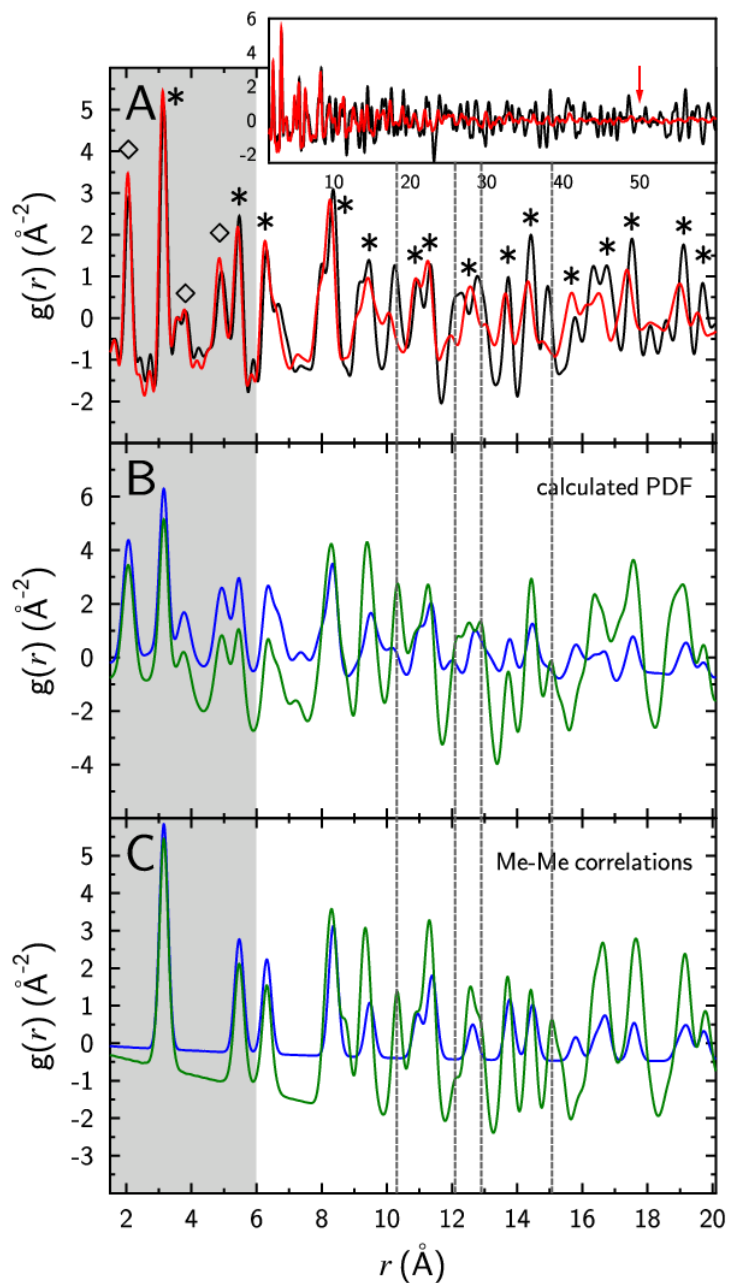
388

389 **Environmental implications.** The importance of anion adsorption in by LDH in general,
390 and green rust in particular, has been highlighted in many studies.^{2,10,26,29,31,64–69} It is also usually
391 acknowledged that the affinity of the interlayer adsorption sites varies as a function of inorganic
392 anions (*e.g.* Cl⁻, NO₃⁻, SO₄²⁻, F⁻, HCO₃⁻/CO₃²⁻), but this comes mostly from analogy with the
393 properties of LDH compounds.^{2,15,26,70} It is thus surprising that so few thermodynamic evaluations
394 of the affinity of interlayer sites for anions were attempted.^{2,15} It is even more surprising that the
395 ion exchange theory was not applied to model LDH reactivity in general and green rust in
396 particular, when considering that LDH are commonly presented as the anionic versions of cationic
397 clays,⁷¹ the natural material for which the ion exchange theory has been the most developed and
398 applied. In this study, the information gathered from time-resolved diffractometric data, TGA and
399 bulk chemistry provided solid evidences that an anion exchange mechanism takes place in green
400 rust interlayers without significant structural changes other than interlayer swelling. We found
401 that the affinity of green rust for SO₄²⁻ compared to Cl⁻ increased with increasing SO₄²⁻ occupancy
402 of the surface sites. This property can be reproduced with a Rothmund and Kornfeld exchange
403 model. Additional experiments with other couples of competing ions and with other green rust
404 samples with a range of substituted cations are now necessary to confirm the suitability of the
405 Rothmund and Kornfeld exchange model to reproduce anion exchange data. Those studies would
406 help to build an anion exchange database for the modeling and prediction of anion adsorption in
407 green rusts present in hydromorphic soils (Fougerite) and engineered settings.

408 FIGURES (Word Style "VA_Figure_Caption").



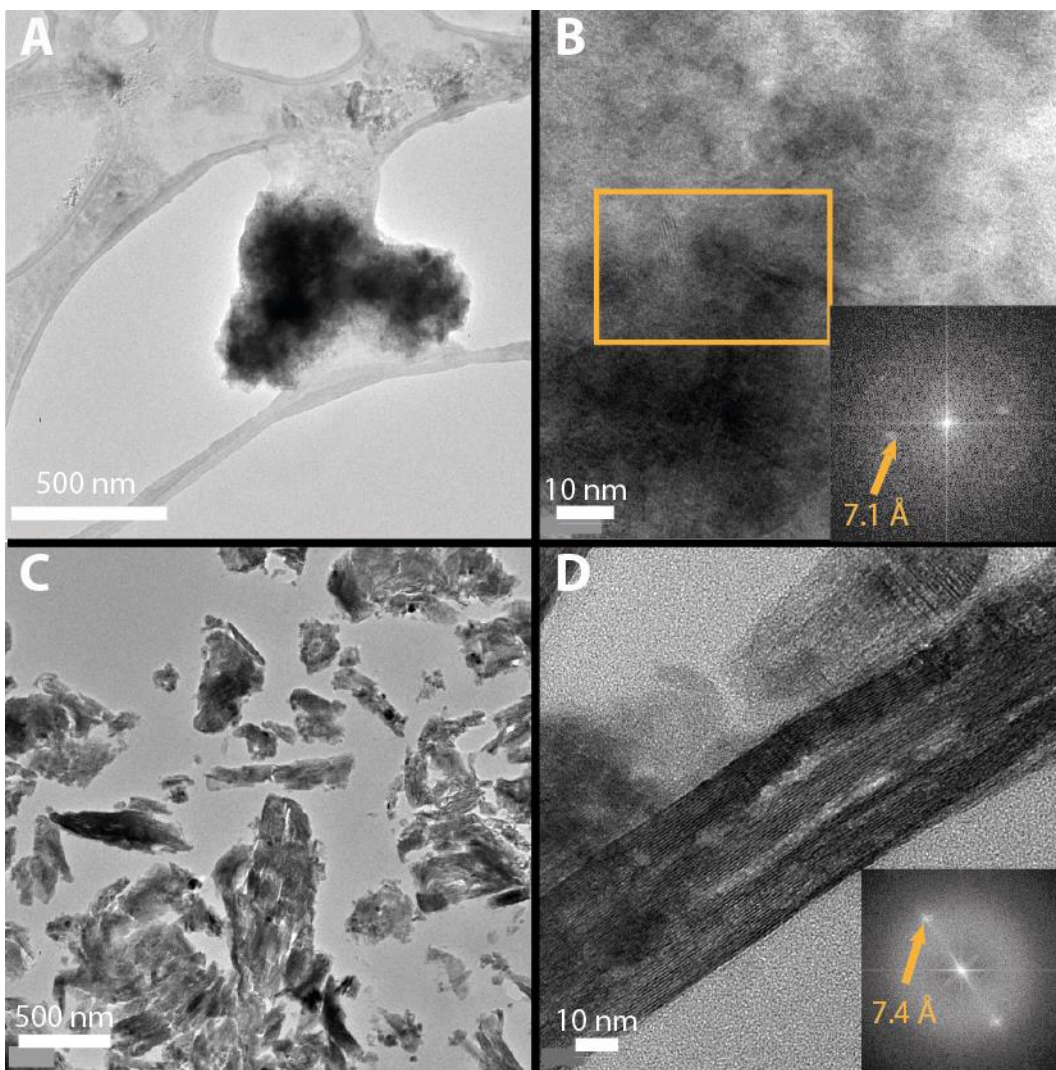
409
410 Figure 1. A: TGA results for nano-GR(Cl). Full line: mass loss (%); Dash line: mass loss derivative
411 (mg·min⁻¹); W_p= interparticle (capillary) pore water; W_{IL}= interlayer water. B: DSC results.
412



413

414 Figure 2: A: PDF data of nano-GR(Cl) (red solid line) and micro-GR(Cl) (black solid line). Inset:
 415 data up to $r = 60 \text{ \AA}$, with the arrow pointing out to the r value at which the PDF from nano-GR(Cl)
 416 is below periodic noise. Main panel: detail of the 1.5-20 \AA region, with indexation of the main
 417 correlations. Me-Me = $\text{Fe}^{2+,3+} - \text{Fe}^{2+,3+}$, $\text{Fe}^{2+,3+} - \text{Co}^{2+}$, or $\text{Co}^{2+} - \text{Co}^{2+}$ correlations (indicated
 418 by a star). Me-O = $\text{Fe}^{2+,3+} - \text{O}$ or $\text{Co}^{2+} - \text{O}$ correlations (indicated by a diamond). B: calculated

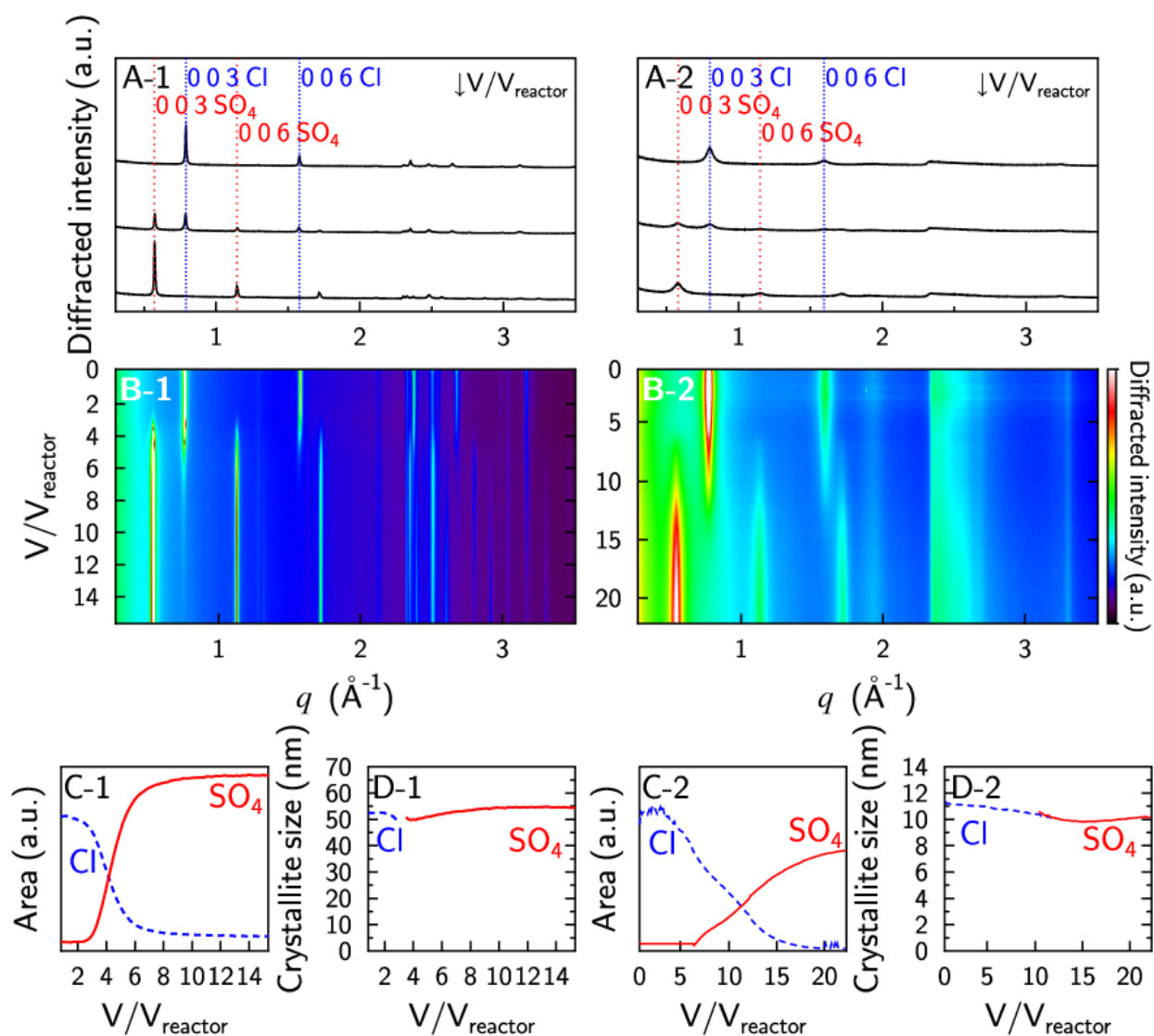
419 PDF for a Fougérite⁷ (green solid line) and for a single Fougérite layer (blue solid line). See main
420 text for details concerning the calculation. C: partial PDF showing only the Me-Me correlations
421 for a Fougérite (green solid line) and a single Fougérite layer (blue solid line). The grey-shaded
422 area corresponds to r values lower than the Me to Me distance in adjacent layers. No data
423 normalization.



424

425 Figure 3. TEM images of nano-GR(Cl) (A, B) and micro-GR(Cl) (C, D). Insert in B: FFT of the
426 area described by the orange box in B. Insert in C: FFT analysis of the whole TEM images in D.

427

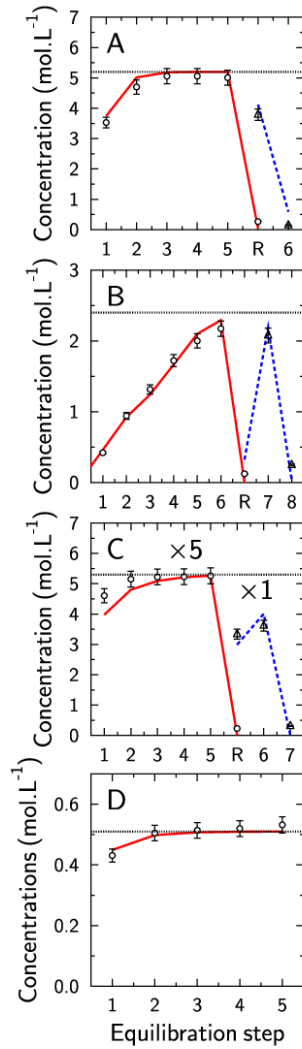


428

429 Figure 4. XRD patterns recorded in-situ during the $5 \text{ mmol}\cdot\text{L}^{-1} \text{ Na}_2\text{SO}_4 / 40 \text{ mmol}\cdot\text{L}^{-1} \text{ NaCl}$
 430 solution flow-through experiment with micro-GR(Cl) (left - 1) and nano-GR(Cl) (right - 2) . A-1:
 431 patterns recorder after 2, 4 and 14 pore volumes (V/V_{reactor}). A-2: patterns recorder after 0, 10 and
 432 20 V/V_{reactor} . B: 2D map of XRD patterns as a function time expressed in pore volumes. C:
 433 Evolution of the 003 peak areas at 0.78 \AA (Cl^- interlayer, blue dash line) and 0.57 \AA (SO_4^{2-}
 434 interlayer, red line) as a function of pore volumes. D: Estimate of the crystallite size as a function
 435 of time inferred from full width at half maximum of the 003 peak and Scherrer equation at 0.78 \AA

436 (Cl⁻ interlayer, blue dash line) and 0.57 Å (SO₄²⁻ interlayer, red line) . Note: the same peak indexing
437 formalism was followed for nano-GR despite the lack of a 3D-ordered structure.

438



439

440 Figure 5. $\text{SO}_4^{2-}/\text{Cl}^-$ exchange data on micro-GR (SO_4^{2-} : circles; Cl^- : triangles). The initial sample

441 was saturated with Cl^- . Steps 1 to 5 (or 6 on figure B) correspond to equilibration with

442 $\text{Na}_2\text{SO}_4/\text{NaCl}$ solutions with total Na concentration of $50 \text{ mmol}\cdot\text{L}^{-1}$. The black dash lines represent

443 the SO_4^{2-} input concentration (the SO_4^{2-} concentration values are multiplied by 5 on figure B). Step

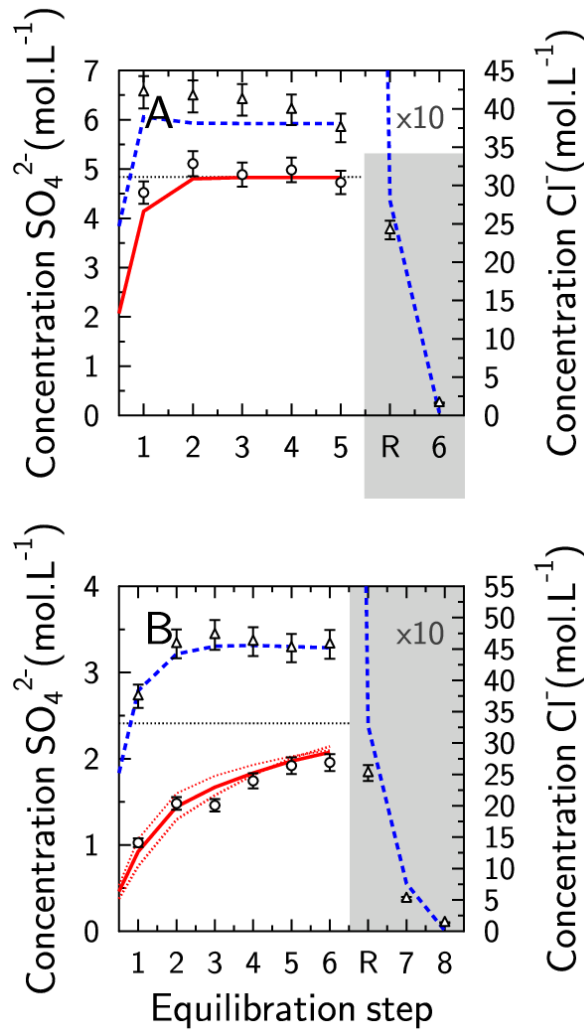
444 R corresponds to the rinsing of the sample with ultrapure water. Steps 6 and 8 correspond to

445 equilibration steps with $25 \text{ mmol}\cdot\text{L}^{-1}$ of Na_2SO_4 (or 7 and 8 on figure B). Red and blue lines

446 represent the results of the Rothmund and Kornfeld exchange model with $\log_{10} K_{ex,RK} = 0.3$ and

447 $\beta = 2.4$. SO_4^{2-} concentrations and blue dashed line is Cl^- concentrations given by the model. The

448 AEC value was taken at $2 \text{ mol}_c\cdot\text{kg}^{-1}$.



449

450 Figure 6. $\text{SO}_4^{2-}/\text{Cl}^-$ exchange data on nano-GR (SO_4^{2-} : circles; Cl^- : triangles). The initial sample

451 was saturated with Cl^- . Steps 1 to 5 (or 6 on figure B) correspond to equilibration with

452 $\text{Na}_2\text{SO}_4/\text{NaCl}$ solutions with total Na concentration of 50 mmol.L $^{-1}$. The black dash lines represent

453 the SO_4^{2-} input concentration. Step R corresponds to the rinsing of the sample with ultrapure water.

454 Steps 6 and 8 correspond to equilibration steps with 25 mmol.L $^{-1}$ of Na_2SO_4 (or 7 and 8 on figure

455 B). Colored lines represent the results of the Rothmund and Kornfeld exchange model with \log_{10}

456 $K_{ex,RK} = 0.2$ and $\beta=5$. The red dotted lines are SO_4^{2-} concentrations from the same model but with

457 $\beta=3$ and $\beta=7$ ($\log_{10} K_{ex,RK} = 0.2$). The AEC value was taken at 1.6 mol.c.kg $^{-1}$. Concentrations of Cl^-

458 from measurements and model are multiplied by 10 in the grey area.

459 TABLES.

460 Table 1. Anion exchange capacity (AEC in mol/kg_{anhydrous GR}) of nano- and micro-GR samples,
461 according to three characterization methods.

Sample	AEC EPMA (Cl ⁻)	AEC EPMA (SO ₄ ²⁻)	AEC Exchange Na ₂ SO ₄
nano-GR	2 ± 0.2	1.8 ± 0.2	1.62 ± 0.2
micro-GR	2.5 ± 0.2	2 ± 0.3	2.0 ± 0.3

462

463

464 AUTHOR INFORMATION

465 Corresponding Author

466 *myriam.agnel@cnrs-orleans.fr -1A Rue de la Ferrollerie, 45071 Orléans – +33 (0) 2 38 64 30 85 –

467 <https://orcid.org/0000-0001-5027-6257>

468 Author Contributions

469 M.A., S.G., and C.T. conceived and designed the exchange experiments. M.A. conducted green
470 rust synthesis and batch exchange experiments. M.A., S.G., F.F., E.E., F.C. and C.T. conducted
471 the synchrotron experiments. F.F., E.E., F.C., M.R. and F.W. contributed materials and analysis
472 tools. M.A., S.G., and C.T. analyzed the data and co-wrote the paper.

473 ACKNOWLEDGMENTS

474 The authors thank Guillaume Wille and Mollud Alleki for assistance with EPMA sample
475 preparation and measurements. S. Grangeon acknowledges funding from the ANR (NACRE—
476 ANR-14-CE01-0006) and Julie Philibert for fruitful discussions. M.I. Agnel acknowledges
477 funding for her PhD from the Région Centre-Val de Loire and Clément Jauvion for constructive
478 discussions. The authors thank the three anonymous reviewer and Prof. Daniel Giammar for their
479 comments and suggestions.

480 SOLEIL and ALBA data were acquired in the frame of proposals 20170391 and 2017022082,
481 respectively.

482 SUPPORTING INFORMATION AVAILABLE.

483 SI_GR_Agnel.pdf (format PDF) – his information is available free of charge via the Internet at
484 <http://pubs.acs.org>. A file containing the Scherrer equation, TGA results, experimental and

485 calculated XRD patterns, results of Rietveld refinement on micro-GR(Cl) and tables with anion
486 exchange experiments data and microprobe results. The main article can be read without this
487 information.

488

489 ABBREVIATIONS

490 GR, green rust; LDH, layered double hydroxide; CoHex, hexammincobalt(III) chloride; EPMA,
491 electron probe micro-analyzes; TGA, thermogravimetric analyses; DTA, differential thermal
492 analysis; XRD, X-ray diffraction; PDF, X-ray Pair Distribution Function; AEC, anion exchange
493 capacity; FFT, Fast Fourier transform.

- 495 (1) Trolard, F.; Bourrié, G. Chapter 5 - Geochemistry of green rusts and Fougerite: A
496 reevaluation of Fe cycle in soils; In *Adv. Agron.*; Academic Press, 2008; Vol. 99, pp. 227–
497 288.
- 498 (2) Usman, M.; Byrne, J. M.; Chaudhary, A.; Orsetti, S.; Hanna, K.; Ruby, C.; Kappler, A.;
499 Haderlein, S. B. Magnetite and green Rust: Synthesis, properties, and environmental
500 applications of mixed-valent iron minerals. *Chem. Rev.* **2018**, *118*, 3251–3304.
- 501 (3) Vodyanitskii, Y. N.; Shoba, S. A. Ephemeral Fe(II)/Fe(III) layered double hydroxides in
502 hydromorphic soils: A review. *Eurasian Soil Sci.* **2015**, *48*, 240–249.
- 503 (4) Abdelmoula, M.; Trolard, F.; Bourrié, G.; Génin, J.-M. R. Evidence for the Fe(II)-Fe(III)
504 green rust “Fougerite” mineral occurrence in hydromorphic soil and its transformation with
505 depth. *Hyperfine Interact.* **1998**, *112*, 235–238.
- 506 (5) Trolard, F.; Abdelmoula, M.; Bourrié, G.; Humbert, B.; Génin, J.-M. R. Mise en évidence
507 d’un constituant de type «rouilles vertes» dans les sols hydromorphes. Proposition de
508 l’existence d’un nouveau minéral: la «fougérite». *Comptes rendus de l’Académie des*
509 *sciences. Série 2. Sciences de la terre et des planètes* **1996**, *323*, 1015–1022.
- 510 (6) Trolard, F.; Génin, J.-M. R.; Abdelmoula, M.; Bourrié, G.; Humbert, B.; Herbillon, A.
511 Identification of a green rust mineral in a reductomorphic soil by Mossbauer and Raman
512 spectroscopies. *Geochim. Cosmochim. Acta* **1997**, *61*, 1107–1111.
- 513 (7) Trolard, F.; Bourrié, G.; Abdelmoula, M.; Refait, P.; Feder, F. Fougerite, a new mineral of
514 the pyroaurite-iowaite group: Description and crystal structure. *Clays Clay Miner.* **2007**,
515 *55*, 323–334.
- 516 (8) Christiansen, B. C.; Balic-Zunic, T.; Dideriksen, K.; Stipp, S. L. S. Identification of green
517 rust in groundwater. *Environ. Sci. Technol.* **2009**, *43*, 3436–3441.
- 518 (9) Hansen, H. C. B.; Kock, C. B.; Nancke-Krogh, H.; Borggaard, O. K.; Sorensen, J. Abiotic
519 nitrate reduction to ammonium: Key role of green rust. *Environ. Sci. Technol.* **1996**, *30*,
520 2053–2056.
- 521 (10) Holmes, A. B.; Gu, F. X. Emerging nanomaterials for the application of selenium removal
522 for wastewater treatment. *Environ. Sci.: Nano* **2016**, *3*, 982–996.
- 523 (11) O’Loughlin, E. J.; Kelly, S. D.; Cook, R. E.; Csencsits, R.; Kemner, K. M. Reduction of
524 Uranium(VI) by mixed Iron(II)/Iron(III) hydroxide (green rust): Formation of UO₂
525 nanoparticles. *Environ. Sci. Technol.* **2003**, *37*, 721–727.
- 526 (12) Su, C. Environmental implications and applications of engineered nanoscale magnetite and
527 its hybrid nanocomposites: A review of recent literature. *J. Hazard. Mater.* **2017**, *322*, 48–
528 84.
- 529 (13) Zegeye, A.; Bonneville, S.; Benning, L. G.; Sturm, A.; Fowle, D. A.; Jones, C.; Canfield,
530 D. E.; Ruby, C.; MacLean, L. C.; Nomosatryo, S.; Crowe, S. A.; Poulton, S. W. Green rust
531 formation controls nutrient availability in a ferruginous water column. *Geology* **2012**, *40*,
532 599–602.
- 533 (14) Bhave, C.; Shejwalkar, S. A review on the synthesis and applications of green rust for
534 environmental pollutant remediation. *Int. J. Environ. Sci. Technol.* **2018**, *15*, 1243–1248.
- 535 (15) Rives, V. *Layered double hydroxides: Present and future*; Nova Science Publishers Inc.,
536 2001; pp. 1–495.
- 537 (16) Sumoondur, A.; Shaw, S.; Ahmed, I.; Benning, L. G. Green rust as a precursor for
538 magnetite: an in situ synchrotron based study. *Mineral. Mag.* **2008**, *72*, 201–204.

- 539 (17) He, Y. T.; Wilson, J. T.; Su, C.; Wilkin, R. T. Review of abiotic degradation of chlorinated
540 solvents by reactive iron minerals in aquifers. *Groundwater Monit. Rem.* **2015**, *35*, 57–75.
- 541 (18) Refait, P.; Génin, J. M. R. The oxidation of ferrous hydroxide in chloride-containing
542 aqueous media and pourbaix diagrams of green rust one. *Corros. Sci.* **1993**, *34*, 797–819.
- 543 (19) Cornell, R. M.; Schwertmann, U. Chapter 13 - Green Rusts; In
544 *Iron Oxides in the Laboratory: Preparation and Characterization*; John Wiley & Sons,
545 2008; pp. 143–145.
- 546 (20) Génin, J. M. R.; Abdelmoula, M.; Ruby, C.; Upadhyay, C. Speciation of iron;
547 characterisation and structure of green rusts and FeII-IIIoxyhydroxycarbonate fougérite. *C.*
548 *R. Geosci.* **2006**, *338*, 402–419.
- 549 (21) Sposito, G. *The thermodynamics of soil solution*; Oxford University Press, 1981; p. 231.
- 550 (22) Peacock, C. L.; Sherman, D. M. Sorption of Ni by birnessite: Equilibrium controls on Ni in
551 seawater. *Chem. Geol.* **2007**, *238*, 94–106.
- 552 (23) Refait, P.; Géhin, A.; Abdelmoula, M.; Génin, J.-M. R. Coprecipitation thermodynamics of
553 iron(II–III) hydroxysulphate green rust from Fe(II) and Fe(III) salts. *Corros. Sci.* **2003**, *45*,
554 659–679.
- 555 (24) Sparks, D. L. Elucidating the fundamental chemistry of soils: Past and recent achievements
556 and future frontiers. *Geoderma* **2001**, *100*, 303–319.
- 557 (25) Refait, P.; Génin, J.-M. . The transformation of chloride-containing green rust one into
558 sulphated green rust two by oxidation in mixed Cl⁻ and SO₄²⁻ aqueous media. *Corros. Sci.*
559 **1994**, *36*, 55–65.
- 560 (26) Trolard, F. Fougérite: From field experiment to the homologation of the mineral. *C.R.*
561 *Geosci.* **2006**, *338*, 1158–1166.
- 562 (27) Fan, G.; Li, F.; Evans, D. G.; Duan, X. Catalytic applications of layered double hydroxides:
563 recent advances and perspectives. *Chem. Soc. Rev.* **2014**, *7040*, 7040–7066.
- 564 (28) Marty, N. C. M.; Grangeon, S.; Elkaïm, E.; Tournassat, C.; Fauchet, C.; Claret, F.
565 Thermodynamic and crystallographic model for anion uptake by hydrated calcium
566 aluminate (AFm): an example of molybdenum. *Sci. Rep.* **2018**, *8*, 7943.
- 567 (29) Barthélémy, K.; Naille, S.; Despas, C.; Ruby, C.; Mallet, M. Carbonated ferric green rust
568 as a new material for efficient phosphate removal. *J. Colloid Interface Sci.* **2012**, *384*, 121–
569 127.
- 570 (30) Caraballo, M. A.; Michel, F. M.; Hochella, M. F. The rapid expansion of environmental
571 mineralogy in unconventional ways: Beyond the accepted definition of a mineral, the latest
572 technology, and using nature as our guide. *Am. Mineral.* **2015**, *100*, 14–25.
- 573 (31) Johnson, C. A.; Murayama, M.; Küsel, K.; Hochella, M. F. Polycrystallinity of green rust
574 minerals and their synthetic analogs: Implications for particle formation and reactivity in
575 complex systems. *Am. Mineral.* **2015**, *100*, 2091–2105.
- 576 (32) Hadi, J.; Grangeon, S.; Warmont, F.; Seron, A.; Greneche, J. M. A novel and easy chemical-
577 clock synthesis of nanocrystalline iron-cobalt bearing layered double hydroxides. *J. Colloid*
578 *Interface Sci.* **2014**, *434*, 130–140.
- 579 (33) Johnson, C. A.; Freyer, G.; Fabisch, M.; Caraballo, M. A.; Küsel, K.; Hochella, M. F.
580 Observations and assessment of iron oxide and green rust nanoparticles in metal-polluted
581 mine drainage within a steep redox gradient. *Environ. Chem.* **2014**, *11*, 377–391.
- 582 (34) Fauth, F.; Boer, R.; Gil-Ortiz, F.; Popescu, C.; Vallcorba, O.; Peral, I.; Fullà, D.; Benach,
583 J.; Juanhuix, J. The crystallography stations at the Alba synchrotron. *Eur. Phys. J. Plus*
584 **2015**, *130*, 160.

- 585 (35) Fauth, F.; Peral, I.; Popescu, C.; Knapp, M. The new Material Science Powder Diffraction
586 beamline at ALBA Synchrotron. *Powder Diffr.* **2013**, *28*, S360–S370.
- 587 (36) Grangeon, S.; Fernandez-Martinez, A.; Claret, F.; Marty, N.; Tournassat, C.; Warmont, F.;
588 Gloter, A. In-situ determination of the kinetics and mechanisms of nickel adsorption by
589 nanocrystalline vernadite. *Chem. Geol.* **2017**, *459*, 24–31.
- 590 (37) Muniz, F. T.; Aurélio, M.; Miranda, R.; Morilla, C.; Santos, D.; Sasaki, J. M. The Scherrer
591 equation and the dynamical theory of X-ray diffraction. *Acta Crystallogr., Sect. A: Found.*
592 *Adv.* **2016**, *72*, 385–390.
- 593 (38) Rodríguez-Carvajal, J. Recent advances in magnetic structure determination by neutron
594 powder diffraction. *Physica B* **1993**, *192*, 55–69.
- 595 (39) Wechsler, B. A.; Lindsley, D. H.; Prewitt, C. T. Crystal structure and cation distribution in
596 titanomagnetites ($\text{Fe}_{(3-x)}\text{Ti}_x\text{O}_4$). *Am. Mineral.* **1984**, *69*, 754–770.
- 597 (40) Egami, T.; Billinge, S. J. L. Chapter 3 The method of total scattering and atomic pair
598 distribution function analysis; In *Underneath the Bragg peaks: structural analysis of*
599 *complex materials*; Pergamon, 2012; Vol. 16, pp. 55–99.
- 600 (41) Grangeon, S.; Fernandez-Martinez, A.; Baronnet, A.; Marty, N.; Poulain, A.; Elkaïm, E.;
601 Roosz, C.; Gaboreau, S.; Henocq, P.; Claret, F. Quantitative X-ray pair distribution function
602 analysis of nanocrystalline calcium silicate hydrates: a contribution to the understanding of
603 cement chemistry. *J. Appl. Cryst* **2017**, *50*, 14–21.
- 604 (42) Ounsy, M.; Girardot, R.; Saintin, K.; Viguier, G. Online data reduction for high throughput
605 beamlines; In *ICALEPCS*; 2013; p. 217.
- 606 (43) Juhás, P.; Davis, T.; Farrow, C. L.; Billinge, S. J. L. PDFgetX3: a rapid and highly
607 automatable program for processing powder diffraction data into total scattering pair
608 distribution functions. *J. Appl. Cryst* **2013**, *46*, 560–566.
- 609 (44) Zhu, M.; Farrow, C. L.; Post, J. E.; Livi, K. J. T.; Billinge, S. J. L.; Ginder-Vogel, M.;
610 Sparks, D. L. Structural study of biotic and abiotic poorly-crystalline manganese oxides
611 using atomic pair distribution function analysis. *Geochim. Cosmochim. Acta* **2012**, *81*, 39–
612 55.
- 613 (45) Shi, C.; Beidaghi, M.; Naguib, M.; Mashtalir, O.; Gogotsi, Y.; Billinge, S. J. L. Structure
614 of nanocrystalline Ti_3C_2 MXene using atomic pair distribution function. *Phys. Rev. Lett.*
615 **2014**, *112*,.
- 616 (46) Parkhurst, D. L.; Appelo, C. A. J. *Description of input and examples for PHREEQC version*
617 *3—A computer program for speciation, batch-reaction, one-dimensional transport, and*
618 *inverse geochemical calculations*; U.S. Geological Survey Techniques and Methods, 2013;
619 p. 497.
- 620 (47) Bond, W. J. On the Rothmund-Kornfeld description of cation exchange. *Soil Sci. Soc. Am.*
621 *J.* **1995**, *59*, 436–443.
- 622 (48) Yun, S. K.; Pinnavaia, T. J. Water content and particle texture of synthetic Hydrotalcite-
623 like layered double hydroxides. *Chem. Mater.* **1995**, *7*, 348–354.
- 624 (49) Miyata, S.; Okada, A. Synthesis of Hydrotalcite-like compounds and their physico-
625 chemical properties - the systems Mg^{2+} - Al^{3+} - SO_4^{2-} and Mg^{2+} - Al^{3+} - CrO_4^{2-} . *Clays Clay*
626 *Miner.* **1977**, *25*, 14–18.
- 627 (50) Palmer, S. J.; Frost, R. L.; Nguyen, T. Thermal decomposition of hydrotalcite with
628 molybdate and vanadate anions in the interlayer. *J. Therm. Anal. Calorim.* **2008**, *92*, 879–
629 886.

- 630 (51) Drits, V. A.; Tchoubar, C. *X-ray diffraction by disordered lamellar structures*; Springer-
631 Verlag, 1990; p. 383.
- 632 (52) Warren, B. E. X-Ray diffraction in random layer lattices. *Phys. Rev.* **1941**, *59*, 693–698.
- 633 (53) Drits, V. A.; Lanson, B.; Gaillot, A.-C. Birnessite polytype systematics and identification
634 by powder X-ray diffraction. *Am. Mineral.* **2007**, *92*, 771–788.
- 635 (54) Grangeon, S.; Lanson, B.; Miyata, N.; Tani, Y.; Manceau, A. Structure of nanocrystalline
636 phyllosulfates produced by freshwater fungi. *Am. Mineral.* **2010**, *95*, 1608–1616.
- 637 (55) Shannon, R. D. Revised effective ionic radii and systematic studies of interatomic distances
638 in halides and chalcogenides. *Acta Crystallogr., Sect. A: Cryst. Phys., Diffr., Theor. Gen.*
639 *Crystallogr.* **1976**, *32*, 751–767.
- 640 (56) Sposito, G. Cation exchange in soils: an historical and theoretical perspective. *ASA Spec.*
641 *Publ.* **1981**, *40*, 13–30.
- 642 (57) Poinssot, C.; Baeyens, B.; Bradbury, M. H. Experimental and modelling studies of caesium
643 sorption on illite. *Geochimica et Cosmochimica Acta* **1999**, *63*, 3217–3227.
- 644 (58) Tournassat, C.; Gailhanou, H.; Crouzet, C.; Braibant, G.; Gautier, A.; Gaucher, E. C. Cation
645 exchange selectivity coefficient values on smectite and mixed-layer illite/smectite minerals.
646 *Soil Science Society of America Journal* **2009**, *73*, 928–942.
- 647 (59) Staunton, S.; Roubaud, M. Adsorption of ¹³⁷Cs on montmorillonite and illite: effect of
648 charge compensating cation, ionic strength, concentration of Cs, K and fulvic acid. *Clays*
649 *and Clay Minerals* **1997**, *45*, 251–260.
- 650 (60) Tremosa, J.; Arcos, D.; Matray, J.-M.; Bensenouci, F.; Gaucher, E. C.; Tournassat, C.;
651 Hadi, J. Geochemical characterization and modelling of the Toarcian/Domerian porewater
652 at the Tournemire underground research laboratory. *Applied Geochemistry* **2012**, *27*, 1417–
653 1431.
- 654 (61) Steefel, C. I.; Carroll, S.; Zhao, P.; Roberts, S. Cesium migration in Hanford sediment: a
655 multisite cation exchange model based on laboratory transport experiments. *Journal of*
656 *Contaminant Hydrology* **2003**, *67*, 219–246.
- 657 (62) Miyata, S. Anion-exchange properties of Hydrotalcite-like compounds. *Clays Clay Miner.*
658 **1983**, *31*, 305–311.
- 659 (63) Tournassat, C.; Bourg, I. C.; Steefel, C. I.; Bergaya, F. Chapter 1 - Surface properties of
660 clay minerals; In *Natural and engineered clay barriers*; Tournassat, C.; Steefel, C. I.;
661 Bourg, I. C.; Bergaya, F., Eds.; Developments in Clay Science; Elsevier, 2015; Vol. 6, pp.
662 5–31.
- 663 (64) Alidokht, L.; Oustan, S.; Khataee, A.; Neyshabouri, M. R.; Reyhanitabar, A. Enhanced
664 removal of chromate by graphene-based sulfate and chloride green rust nanocomposites. *J.*
665 *Taiwan Inst. Chem. Eng.* **2016**, *68*, 266–274.
- 666 (65) Christiansen, B. C.; Geckeis, H.; Marquardt, C. M.; Bauer, A.; Römer, J.; Wiss, T.; Schild,
667 D.; Stipp, S. L. S. Neptunyl (NpO₂⁺) interaction with green rust, GRNa₂SO₄. *Geochim.*
668 *Cosmochim. Acta* **2011**, *75*, 1216–1226.
- 669 (66) Mitsunobu, S.; Takahashi, Y.; Sakai, Y.; Inumaru, K. Interaction of Synthetic Sulfate Green
670 Rust with Antimony(V). *Environ. Sci. Technol.* **2009**, *43*, 318–323.
- 671 (67) Ona-Nguema, G.; Morin, G.; Wang, Y.; Menguy, N.; Juillot, F.; Olivi, L.; Aquilanti, G.;
672 Abdelmoula, M.; Ruby, C.; Bargar, J. R.; Guyot, F.; Calas, G.; Brown, G. E. Arsenite
673 sequestration at the surface of nano-Fe(OH)₂, ferrous-carbonate hydroxide, and green-rust
674 after bioreduction of arsenic-sorbed lepidocrocite by *Shewanella putrefaciens*. *Geochim.*
675 *Cosmochim. Acta* **2009**, *73*, 1359–1381.

- 676 (68) Randall, S. R.; Sherman, D. M.; Ragnarsdottir, K. V. Sorption of As(V) on green rust
677 (Fe₄(II)Fe₂(III)(OH)₁₂SO₄ · 3H₂O) and lepidocrocite (γ-FeOOH): Surface complexes from
678 EXAFS spectroscopy. *Geochim. Cosmochim. Acta* **2001**, *65*, 1015–1023.
- 679 (69) Wang, Y.; Morin, G.; Ona-Nguema, G.; Juillot, F.; Guyot, F.; Calas, G.; Brown, G. E. J.
680 Evidence for different surface speciation of arsenite and arsenate on green rust: An EXAFS
681 and XANES study. *Environ. Sci. Technol.* **2010**, *44*, 109–115.
- 682 (70) Hansen, H. C. B.; Guldberg, S.; Erbs, M.; Bender Koch, C. Kinetics of nitrate reduction by
683 green rusts—effects of interlayer anion and Fe(II):Fe(III) ratio. *Appl. Clay Sci.* **2001**, *18*,
684 81–91.
- 685 (71) Forano, C.; Costantino, U.; Prévot, V.; Gueho, C. T. Chapter 14.1 - Layered Double
686 Hydroxides (LDH); In *Handbook of Clay Science*; Bergaya, F.; Lagaly, G., Eds.;
687 Developments in Clay Science; Elsevier, 2013; Vol. 5, pp. 745–782.
688